The sintering behavior of ultrafine alumina particles

John E. Bonevich[a] and Laurence D. Marks
Department of Materials Science and Engineering, Northwestern University, 2145 Sheridan Road, Evanston, Illinois 60208

(Received 22 July 1991; accepted 18 February 1992)

Ultrafine particles (UFPs) of aluminum oxide were prepared by an arc discharge, sintered in a custom-built ultrahigh vacuum (UHV) furnace system, and characterized in a high resolution electron microscope (HREM) operating under UHV conditions. The UFPs produced range in size from 20 to 50 nm and have highly faceted surfaces. The atomic structure of the UFPs corresponds to the cubic (γ) and orthorhombic (δ) variants of the spinel structure. Sintering in these UFPs demonstrates three major issues. Surface faceting plays a major role in determining the final sintering geometry with sintering occurring predominantly on the close-packed {111} facets. Surface diffusion is the predominant mechanism for sintering, as evidenced by the fact that many sintered particles have their initial adhesion structure 'locked-in' during sintering with no reorientation occurring. Furthermore, the necks formed during sintering have well-defined, atomically sharp contact angles which suggests that the neck growth process is controlled by the faceted structures and may be modeled by a mechanism similar to crystal growth due to ledges, grain boundaries, and twins. The driving force for sintering can be considered as a chemical potential difference between facet surfaces and the neck region.

I. INTRODUCTION

Ceramics are materials of extreme technological importance, prized for their chemical resistivity, hardness and wear resistance, high melting temperature, and low densities. And yet, the widespread application of these materials has been impeded by their sensitivity to mechanical and thermal shocks as a result of their brittle nature. The relatively poor mechanical properties are usually considered to be the consequence of flaws within the materials which lead to catastrophic failure. Whereas metals may plastically deform, either by the motion of lattice dislocations[1] or diffusional creep,[2] materials with immobile lattice dislocations are brittle at low temperatures where diffusional creep is inoperative.

In recent developments,[3] ceramic materials have been tailored to accommodate diffusional creep at low temperatures. This is achieved by making the grain size of the polycrystalline ceramic on the order of a few nanometers (nm), hence the name nanocrystalline materials. Nanocrystalline materials may deform plastically under an applied stress due to the ease with which the small grains slide past each other.

Another way to view the behavior of nanocrystalline materials is through an analogy to the Hall–Petch[4,5] relationship in metals which states that the yield stress is related to the grain size as:

$$\sigma = \sigma_0 + f d^{-1/2} \qquad (1)$$

where σ is the yield stress, σ_0 the lattice friction stress required to move individual dislocations, f a constant, and d the spatial grain size. According to this relationship, a material with grain size of a few nms should possess improved mechanical properties over a bulk material with grain sizes of several microns.

In the structural regime between bulk ceramic materials and the novel nanocrystals are the ultrafine-grained materials, i.e., grain sizes about 20–50 nm. Thus, it is conceivable that these ultrafine-grained materials could represent a sort of amalgam, possessing both the advantageous properties of conventional bulk ceramics and the unique and desirable qualities of the nanocrystalline materials. Given that ultrafine-grained ceramic powders can be easily produced, the central questions one has to address are, what is the behavior of these particles as they sinter at elevated temperatures, and can this sintering process be understood on an atomic level. In this paper the process of sintering in ultrafine particles (UFPs) of ceramic materials will be investigated in terms of both the atomic structure and particle shape considerations.

Nanocrystalline materials have been previously investigated by electron microscopy techniques. Siegel *et al.*[6] studied the properties and structure in consolidated TiO_2 specimens prepared by the gas-condensation method and reported rapid densification rates at sintering temperatures much lower than those expected for coarse-grained materials. The structure of nanocrystalline Pd was studied by high resolution electron microscopy (HREM) with the result that the grain boundaries were narrow (0.5 nm) and were not observed to be

[a]Present address: Hitachi Advanced Research Laboratory, Hatoyama, Saitama 350-03, Japan.

randomly ordered.[7] In contrast, Wunderlich *et al.*[8] did find that the grain boundary region in nanocrystalline Pd was substantially different from that observed in bulk polycrystalline samples. The interpretation for this result was that the extended boundary region was in a high energy state with entropies comparable to that of a gaseous material.

Previous HREM studies of the sintering behavior in UFPs were conducted by Iijima[9,10] and Warble.[11] These researchers independently produced UFPs of aluminum oxide by arc discharge methods for their sintering experiments. Iijima noticed the formation of new alumina phases and sintered the UFPs under vacuum at 1350 °C for 2 h. A few examples of sintering were shown and the resulting interfaces (grain boundaries) between particles were considered to be atomically irregular. Warble sintered UFPs of alumina at atmosphere at 1150 °C for 48 h and noted that the γ-phase particles had transformed to the α-phase in a "plate and block" arrangement.

In all of the preceding discussion, no mention was made concerning the role of impurities on the properties of these materials. However, the large surface-to-volume ratios found in the UFPs and the fact that many properties are surface-controlled mandates that the extrinsic effects of impurities be carefully scrutinized. For instance, there is considerable debate over whether the Hall–Petch relation can be extended down to grain sizes typically found in UFPs and nanocrystalline materials. Nieman *et al.*[12–14] have reported that nanocrystalline Cu and Pd samples have improved mechanical properties over coarse-grained materials and that no appreciable grain boundary diffusional creep was observed. However, Chokshi *et al.*[15] have contradictory evidence in nanocrystalline Cu and Pd reporting a *negative* Hall–Petch relationship and substantial diffusional creep resulting in grain boundary sliding.

Contamination is almost certainly the defining factor in the discrepancy between these results as the materials systems are the same, and the samples are presumably prepared and tested in a similar manner. The impurities in these systems may act to either 'embrittle' or 'lubricate' the grain boundaries in these nanocrystalline materials; i.e., the behavior is controlled by extrinsic properties. The existence of impurities can also have a dramatic effect on the thermodynamics of surfaces and the rates of surface diffusion.[16] For example, adsorption on surfaces can result in a negative surface stress.[17]

In no previous study of UFP sintering behavior have the issues presented by contamination been adequately handled. Iijima[10] did mention that the vacuum level present during observation of the UFPs was about 10^{-6} Pa. However, the important factor is not the overall vacuum level, but the *cleanliness* of the entire system; this will control the observed behavior. From the onset of this study, a determined effort was made to ensure the cleanliness of the entire ultrahigh vacuum (UHV) system, which includes a furnace, a transfer system, and a UHV-HREM. The goal here was at least to minimize, if not to eliminate completely, any contaminating species (the major impurities include hydrocarbons from pump oils and the atmosphere) during the particle formation and sintering processes. In this paper, we present the sintering behavior of alumina UFPs conducted in a clean environment. In contrast to HREM studies of consolidated nanocrystalline materials, which must be prepared by mechanical thinning and ion-milling techniques, the UFPs are quite amenable to investigation by HREM as they are electron transparent and one is able simultaneously to view both particle surface and "bulk" structures.

II. EXPERIMENTAL METHOD

The alumina UFPs were produced by the arc discharge method whereby an arc is struck between two high purity aluminum electrodes in an atmosphere of Ar–20% O_2. The UFPs formed as a result of this process have highly faceted surfaces[18] which is consistent with earlier observations.[19–23] The UFPs range in size from 20 to 50 nm and agglomerate in short chain-like clusters. These chains were carried by the arcing gas into a furnace tube where they sintered and were then collected onto an electron microscope specimen cartridge for structural characterization. The details of the custom-designed UHV furnace, shown schematically in Fig. 1, are discussed elsewhere.[24] However, it is sufficient to mention that the UHV furnace system allows one to produce, sinter, collect, and transport the UFP specimens under clean conditions. The Hitachi UHV-H9000 HREM used to characterize the structure of the UFPs has also been described in detail elsewhere.[25] The UHV-HREM has an operating pressure of 2×10^{-8} Pa at the specimen, and the furnace system achieves UHV levels of 4×10^{-7} Pa.

The following method was used to obtain sintered specimens. First, the UHV chambers of the furnace system were baked in order to achieve the ultimate vacuum. Then, under vacuum, the furnace tube was energized to the desired temperature all the while monitoring the cleanliness of the system with a residual gas analyzer. Once the desired temperature was reached, the furnace was back-filled with the arcing gas to the appropriate pressure and the gas was then forced to flow up the furnace tube. After the desired steady-state flow rate (which determined the sintering time) and temperature were obtained, the arc was started and the UFPs were carried by the flowing gas into the furnace tube. The microscope specimen cartridge was then positioned in the UFP/gas stream. After sufficient collection time ($\sim$5 min), the furnace system was re-evacuated to 10^{-6} Pa within an

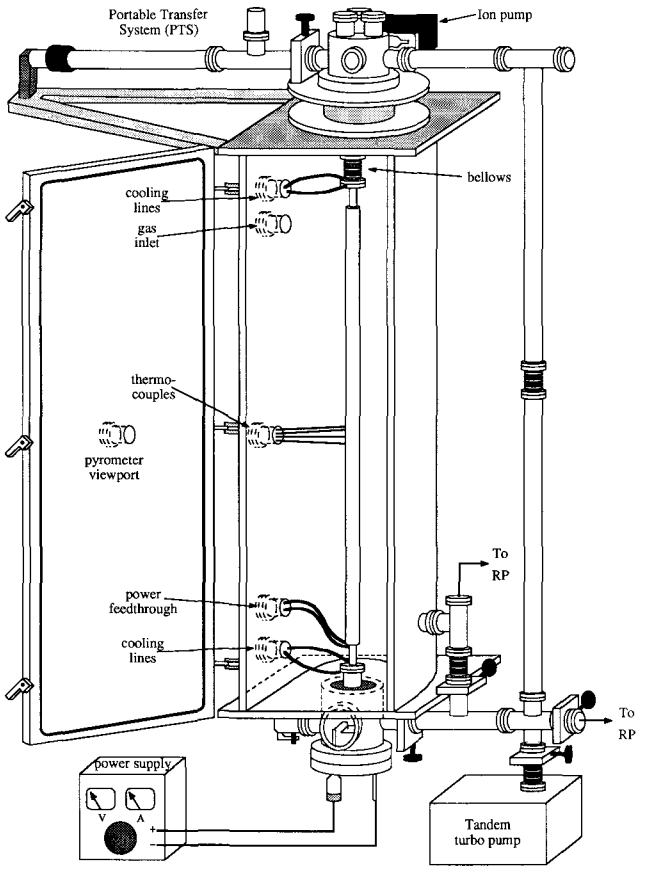

FIG. 1. Schematic diagram of the UHV furnace system showing the arcing chamber (at bottom), the furnace tube (center), and the collection chamber with the transfer system attached (at top). The furnace tube is contained within the large vacuum chamber shown with its O-ring sealed door opened. The whole structure rests upon an angle-iron frame which is not shown. During experiments, the Ar–20% O_2 gas is admitted to the arcing chamber, forced to flow up through the furnace tube where sintering occurs, and then the specimens are collected on the microscope cartridge.

hour. The specimen manipulator was retracted into the portable transfer system (PTS) which was gate valve sealed and had a battery-powered ion pump. The PTS was then detached from the furnace and transported to the UHV-HREM.

III. ATOMIC STRUCTURE

The arc discharge production of UFPs, consistent with other methods, results in a wide variety of nonequilibrium phases. In fact, it would be fair to say that there are nearly as many alumina phases as there are Greek letters with which to name them. Nevertheless, we can classify various phases into specific groups based on some simple structural units. For example, if we consider that γ-alumina can be made by the calcination of boehmite (aluminum hydroxide), we can then follow the transformation of γ- to α-alumina as a function of temperature:

$$\gamma \quad (750\ ^\circ\mathrm{C}) \rightarrow \delta \quad (1000\ ^\circ\mathrm{C}) \rightarrow \theta \quad (1250\ ^\circ\mathrm{C}) \rightarrow \alpha \tag{2}$$

where the γ and δ phases (loosely used names) are based upon the cubic spinel structure, the θ phase on monoclinic units, and the well-known α is rhombohedral (hexagonal). While the α-phase (corundum) has only one well-defined structure, the lower temperature phases have many structural variants and therefore are labeled here in a very loose fashion, though it is not entirely correct to do so.

A review of the published literature on transition-phase aluminas reveals a wide variety of structures that fall into the γ- and δ-alumina classification. Though there are many 'cubic' phases,[26] the most widely cited γ-phase is that of Rooksby,[27] who determined that the spinel structure[28] with lattice parameter of 0.79 nm and space group O_H^7–$Fd3m$ was correct.

The δ-phase of alumina is also based upon the spinel structure and, being a variant of γ, has a number of structural possibilities. Tetragonal variants have been reported[29–32] with cell parameters of approximately 0.796 and 1.17 nm. These structures have the common element that they differ from the cubic spinel by the introduction of antiphase boundaries (APB) in order to accomplish the 3/2 expansion of the cubic unit cell. The δ-phase of alumina has also been reported[10,33] to be orthorhombic with unit cell dimensions of $2a_\gamma$, $3/2a_\gamma$, and a_γ where a_γ is the cell parameter of the cubic γ-alumina. These structures also required the introduction of APBs along the 3/2 {010} planes and it was noticed[33] that there was substantial ordering of the tetrahedral sites.

It is an important point to note that with spinels the crystal form is $T^{2+}(M^{3+})_2O_4$ where the oxygens form an fcc close-packed arrangement and T and M indicate the tetrahedrally and octahedrally coordinated cation species as in $MgAl_2O_4$ (normal spinel). However, with the aluminas we can make no distinction between the different valence states of the cations in order to determine the true structure as can be done in the case of magnetite, Fe_3O_4.[34] The only recourse available is to assign occupancies to different sites in the lattice to match the experimentally observed images,[35] i.e., standard HREM. For instance, in the fully disordered γ-spinel octahedral sites would have an occupancy of unity, whereas the tetrahedral sites are only two-thirds occupied in a random fashion to maintain the proper stoichiometry of Al_2O_3 or $(Al^{3+})_{2/3}(Al^{3+})_2O_4$.

IV. RESULTS

The UFPs observed in this study consisted of both the γ- and δ- aluminas based on the spinel structure. Figure 2 is a typical example of a γ-alumina aligned

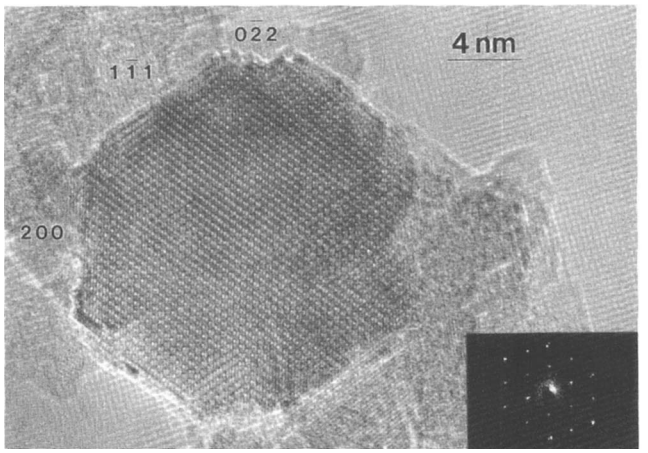

FIG. 2. Example of a γ-alumina UFP oriented along the [011] zone with highly faceted surfaces. The {220} facets, being unstable with respect to the Wulff construction, have decomposed into {111}-type 'nanofacets'. The inset is an optical diffractogram (ODM). Note: the δ-phase which is based on the cubic γ has very similar particle shapes.

along the [011] zone axis. The particle shape is highly faceted with the low-index {111} and {200} surfaces predominating. (Note: the δ-phase based on the cubic γ has very similar particle shapes.) The structure of the γ-phase can be modeled in the following manner: the spinel structure is assumed, from Rooksby,[26] where the aluminum cations on octahedral sites have full occupancy and the tetrahedral cations are only partially occupied. In order to simulate an HREM image of this γ-alumina it is necessary to treat all of the tetrahedral sites (excluding the seven-eighths having zero occupancy) as equally occupied. That is, a random distribution of vacancies is imposed resulting in all tetrahedral sites being two-thirds occupied.

Analysis of the measured interplanar spacings results in a lattice parameter for γ-alumina of 0.79 ± 0.01 nm. This agrees well with the previously observed structures although there are indications that our γ-phase may in fact be slightly tetragonal. Consider, for example, that one set of {111} spacings corresponds to 0.46 nm which gives a unit cell lattice parameter of 0.8 nm. Another set of {111} planes measures 0.45 nm which would correspond to a lattice parameter of 0.78 nm. These measurements fall within the experimental error; however, the presence of distortions in the spinel structure due to defects certainly is plausible as is the case with our δ-alumina.

Delta alumina

The δ-phase of alumina was also observed in many of the arc discharge powders. In fact, the results of x-ray powder diffraction conducted on unsintered powders from the smoke[36] revealed that the δ-phase was the majority phase, comprising some 60% of the sample with 40% γ-phase. The δ-phase, as mentioned earlier, is a variant of the spinel structure and so many of the x-ray reflections from both γ- and δ-phases overlap. But whereas the x-ray results must be interpreted carefully, the HREM images and diffraction patterns (DPs) of δ-alumina clearly show the expansion of the unit cell. As a result of DP analysis, the lattice parameters of the δ-phase were determined to be $a_\delta = 1.58$ nm, $b_\delta = 1.17$ nm, and $c_\delta = 0.79$ nm. These values, while similar to those previously reported,[9,10,33] represent an $\approx$4% contraction of the unit cell. However, the c_δ dimension (cubic basis) does agree with the x-ray literature. The dimensions of this δ-phase were confirmed by examining the phase along different crystal orientations. Consider Fig. 3 which shows the image and DP of a large particle of δ-alumina where the zone axis corresponds to $[102]_\delta$. When one examines the DP, it is apparent from the strong intensity reflections that the $[102]_\delta$ is structurally similar to the $[101]_\gamma$ orientation. In fact, the similarity is as follows: $(400)_\gamma$ is synonymous with $(060)_\delta$ and $(202)_\gamma$ with $(44\bar{2})_\delta$.

In addition to having interplanar spacings consistent with this δ-phase the DP in Fig. 3 was taken under 'converged-beam' conditions. That is, the electron beam was focused to the smallest probe attainable under normal HREM conditions. These conditions allow one to use the intensities of the DP to determine the most probable space group of the diffracting crystal. From the DP it is apparent that two possible space groups are $P2_12_12$ or $P2_12_12_1$ which is also consistent with earlier structural determinations.

V. SINTERING PROCESS

Once the UFPs have been structurally characterized, we may then turn our attention to the process of sintering in the UFPs. There were three controllable variables in this sintering study: the particle size, the sintering temperature, and the sintering time (the residence time of particles within the furnace). Further information on the relationships among the pressure, temperature, and flow rate in the UHV furnace system will be described elsewhere.[37] In order to elucidate the general sintering trends, the sintering times and temperatures were varied, holding the particle size distribution constant.

A. Sintering at low temperatures

Figure 4 is a typical example of two particles that have sintered together under conditions of 1000 °C and a dwell time of 0.10 s. It shows the random manner in which the UFPs adhere and sinter to each other. The central particle, $[123]_\gamma$ orientation, has a well-defined facet structure and has sintered to another particle where the resultant neck/grain boundary region can be considered as atomically rough. The particle also shows the 'dark-line' facets[38,39] typical of the γ-phase.

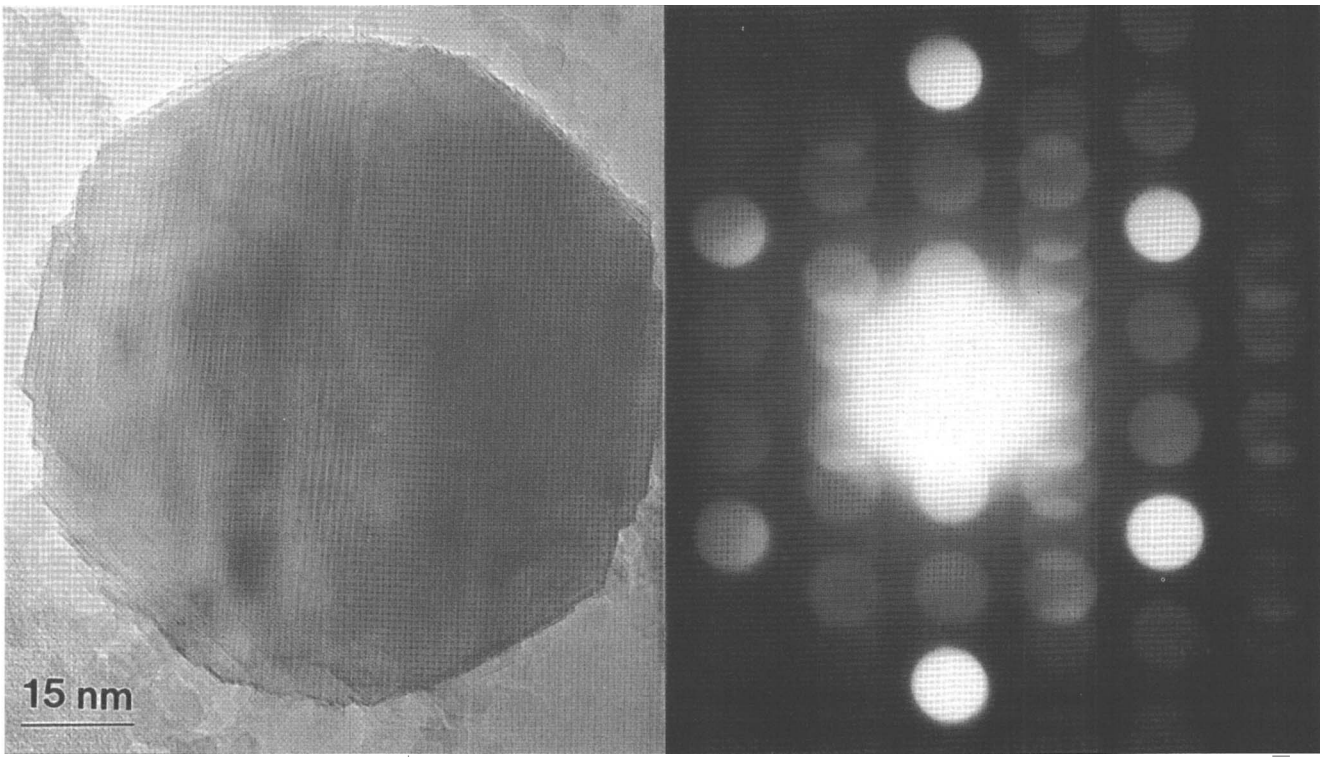

FIG. 3. (a) Image and (b) diffraction pattern (DP) of a large particle of δ-alumina oriented near the [102] zone axis. The particle has highly faceted surfaces and from the DP can be classified into the $P2_12_12$ or $P2_12_12_1$ space groups.

The UFPs form long chains before entering the furnace to sinter; Figs. 5 and 6 illustrate the results. Here, three of a many-particle chain have been imaged revealing atomically rough neck regions along specific facets and discrete contact angles. In addition, it is clearly evident that the particles have adhered to each other and sintered with no apparent 'reorientation' of the sintered particles to form low energy interfaces. This result indicates that surface diffusion is sufficiently fast that the initial contact orientation is 'locked-in' before significant neck growth occurs. Furthermore, Fig. 6 shows the presence of sintered necks of mixed facet type (i.e., {220} to {111}) giving atomically rough interfaces.

An apparent contradiction of the no reorientation argument can be found in Fig. 7 where two particles have sintered. Here, instead of a seemingly random

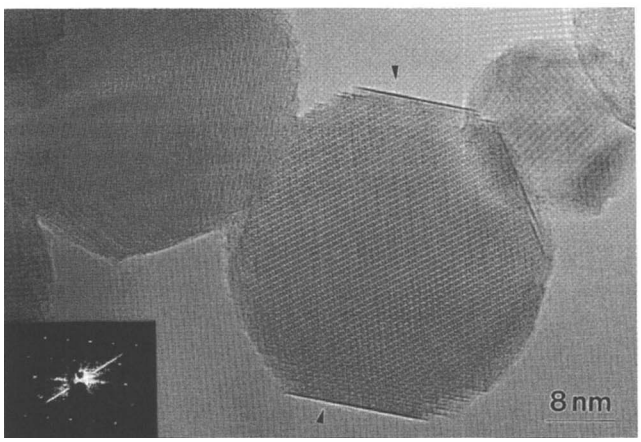

FIG. 4. A sintered particle, under conditions of 1000 °C and 0.10 s, which is aligned along the $[123]_\gamma$ orientation. The dark-line facets (arrowed), characteristic of the γ-phase, are identified as {111} surfaces.

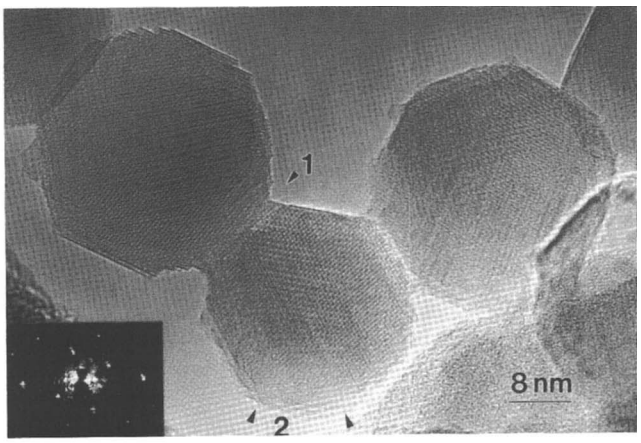

FIG. 5. Chain of sintered particles. Here, the particles have adhered with no reorientation occurring. The resulting wedged gap between the particles (arrow 1) was filled in by surface diffusion. The middle particle's far side (arrow 2) appears to have roughened surfaces as a result of mass transport to the neck regions.

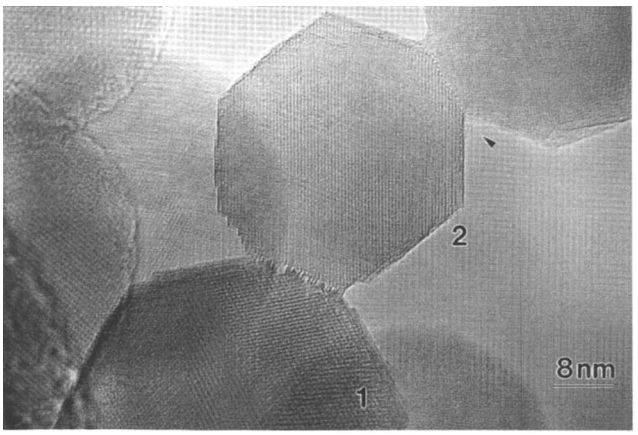

FIG. 6. Chain of sintered particles where the neck regions can be considered as atomically irregular. The middle particle (#2) has a distorted shape (arrowed) with respect to the Wulff construction as a result of the sintering process. Furthermore, the {220} facet of particle 1 is sintered to the {111} facet of particle 2, giving an atomically irregular interface.

orientation, the two particles appear to have a high degree of coherency corresponding to the $\{311\}_\gamma$ planes. These planes have an approximately 5° misorientation which has led to a low angle grain boundary. It may be speculated that since the particles do not have the well-defined facets as in previous examples, and appear more spherical, that the particles were able to 'roll around' on their surfaces until this orientation was achieved.

Figures 8, 9, and 10 illustrate the sintering results when the flow rate was slowed to a dwell time of 0.27 s at 1000 °C. In the case of Figs. 8 and 9, the sintering process was definitely confined to the {111} facets for *all* sintered particles and the contact angles in the neck have remained discrete despite the longer sintering time. One notable feature in Fig. 9 is that the sintered particles appear to have a neck region which is clearly dis-

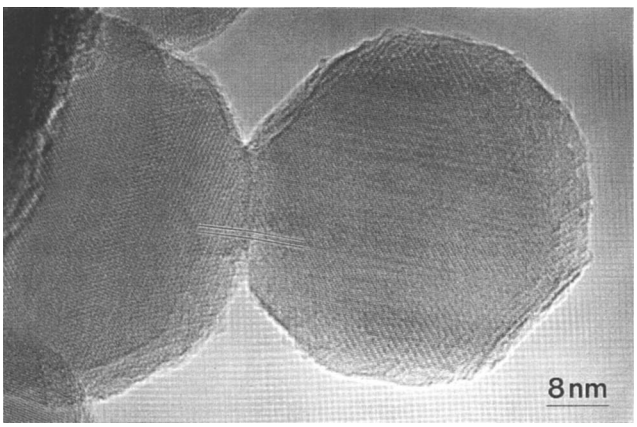

FIG. 7. Two particles that have sintered with a 5° misorientation of their {311} planes (fringes parallel to lines). These spherical particles were able to "roll around" to achieve this orientation.

FIG. 8. Many-particle system where all particles have sintered on their {111} facets. Note the discrete contact angles of all the necks.

cernible from the particles themselves—an unexpected result. Given that the driving force is a reduction in surface energy, one would expect the particle centers to approach each other during the sintering process. The question then becomes why the particles, rather than freely approaching each other, remained apart. One

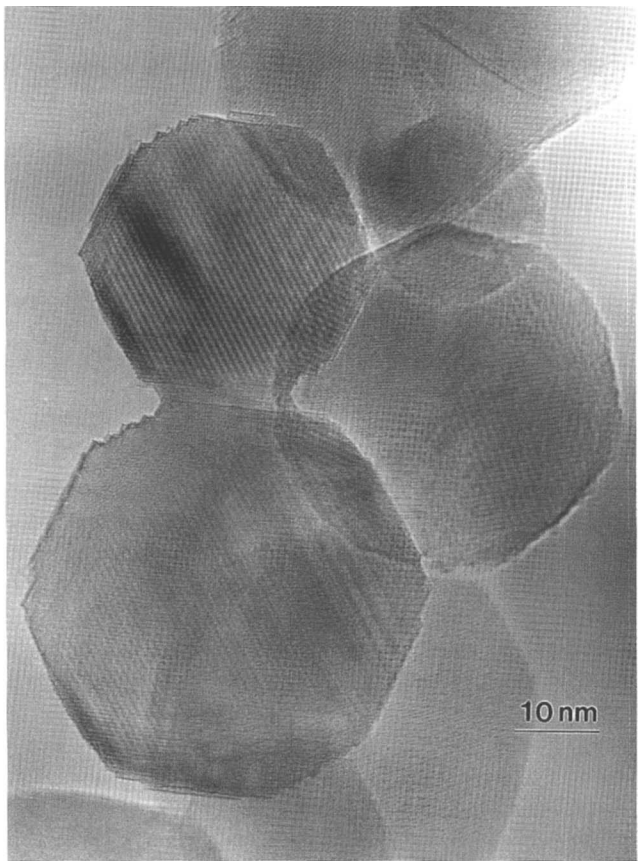

FIG. 9. Two sintered particles that were constrained by a third particle. Though all the interfaces cannot be seen directly, it is reasonable to assume that all three particles have sintered together. The extended grain boundary region is distinct from the two particles.

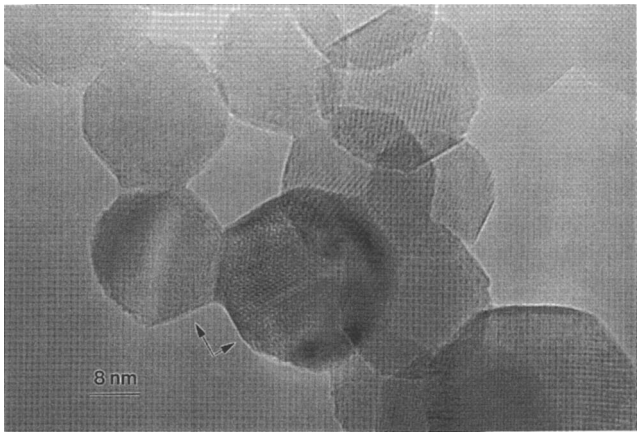

FIG. 10. Many particles that have sintered and are constrained from consolidating. The central particle is the oriented along the $[100]_\delta$ zone and shows the 3/2 expansion of the spinel unit cell. The [010] (long) and [001] (short) directions are shown as arrows.

must note, however, that the particles were not free to approach each other as they were constrained by a third particle beneath them. Though the inference is indirect, Occam's razor would dictate the assumption that if the two particles have sintered to each other, it is reasonable to expect them also to be sintered to the third particle. Thus, in this case, the neck region may have formed as the result of step growth from a facet surface to fill in the open space between the particles. Figure 10 is an example of sintering occurring in a many-particle system where the particles have fully developed neck structure. In this case, the extensive interconnectivity between the particles has prevented substantial consolidation–for example, the five-particle pore as shown. The central particle in Fig. 10 is a good example of the [100] orientation of the δ-phase which shows the 3/2 expansion of the spinel lattice.

B. Sintering at high temperatures

When the temperature of sintering was increased to 1200 °C, keeping the sintering times and particle size constant, the processes discussed above were accelerated. Consider Fig. 11 where four particles have sintered together. Consistent with earlier examples, the sintering occurred on well-defined facets with discrete contact angles. However, attention must be focused on the particle that appears to have undergone substantial particle/grain growth, as indicated by the outlined region. Furthermore, the neck region as a result of this particle growth has considerably different contrast than either sintered particle. This result lends credence to the notion that there exists a distinct grain boundary region that has no direct structural relationship to either sintered particle, though it may be compositionally identical. In fact, the fringe spacings in the boundary region correspond to

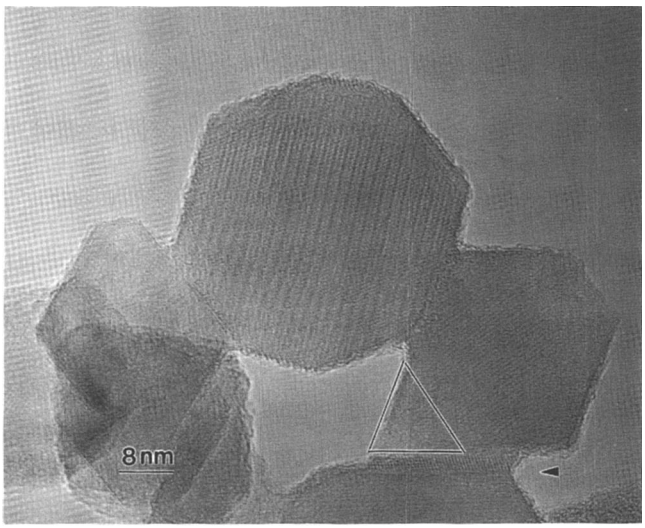

FIG. 11. Many-particle system where all particles have sintered at 1200 °C. One particle has experienced 'grain' growth, as outlined, and has a quite distinct grain boundary region. The fringe spacing of the arrowed boundary region corresponds to the $\{111\}_\gamma$ planes. Note the presence of surface roughening due to the higher sintering temperature.

the 0.46 nm $\{111\}_\gamma$ interplanar spacing which implies a structural rotation of the crystal in the boundary region.

C. Bright-field/dark-field analysis

The dark-field analysis of the sintered specimens revealed that there was little strain induced by the contact between sintered particles; a typical example is shown in Fig. 12. Instead, the stress due to adhesion seems to be accommodated by considerable internal faulting within the particles. These results are in contrast with those of Thölen[40,41] where significant strain fields occurred during adhesion in small metallic particles. Whereas the metal particles were able to deform plastically in response to the contact stress, the ceramic particles cannot alleviate the stress in this fashion and instead internally fault. These results, however, are consistent with those of Marks[42] where it was noted that virtually all of the strains evident in small metal particles were inhomogeneous in nature and that the strains induced the formation of multiply-twinned particles (MTPs). One should also note in the bright-field images the considerable surface roughening as a consequence of long (20 min) doses of low flux electron irradiation necessary for BF/DF work.

D. Phase transformations

The UFPs entering the furnace traverse a temperature profile which, in addition to promoting sintering and neck growth, can lead to phase transformations, e.g., γ to δ. Consider, for example, Fig. 13 where a particle was sintered to a smaller particle. If one traces the general outline of each particle shape, then one would

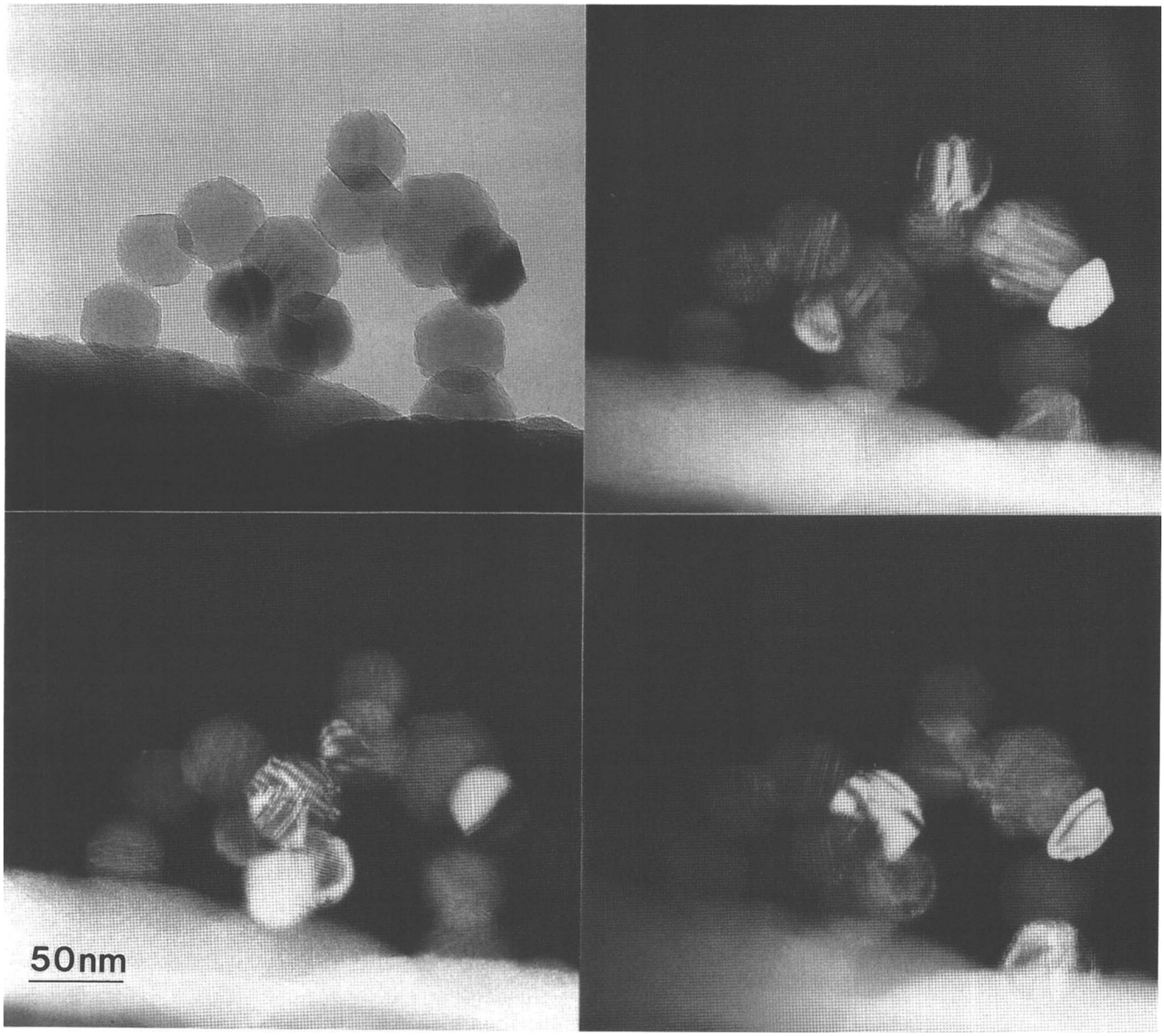

FIG. 12. Bright-field/dark-field montage of sintered particles. The particles show a high degree of internal faulting and twinning as a result of particle adhesion. Note the considerable surface roughening in the BF image due to low-flux irradiation.

expect to find the grain boundary in between them. Instead, the 'interface' between the particles appears to be completely commensurate and the grain boundary has moved up into the smaller particle. An interpretation of this result is that the particles entered the furnace with the γ structure and underwent a phase transformation to the δ-phase. Consequently, the grain boundary migrated into the smaller particle in order to reduce overall interfacial energy. One might speculate that given sufficient time, the grain boundary would have completely migrated through the particle, leaving a single grain in the shape of the original two particles.

Conversely, one might interpret Fig. 13 as being the result of only grain boundary migration without the need to invoke a phase transformation. Consider the case of two adhered δ-phase particles where the smaller particle was highly misoriented relative to the larger particle. Then, as a result of the elevated sintering temperatures, the initial grain boundary could nucleate growth in the smaller particle so as to regrow it in an epitaxial fashion. This would then explain why one side of the small particle appears 'amorphous' in structure; it is simply so misoriented that no structural periodicities were imaged. It should be mentioned that all particles produced from the arc discharge were crystalline (and not amorphous), so that this explanation seems to be the most probable one, though a phase transformation cannot be definitively ruled out.

Figure 14 illustrates the existence of statistical anomalies in the sintering of UFPs. Here two twinned γ-

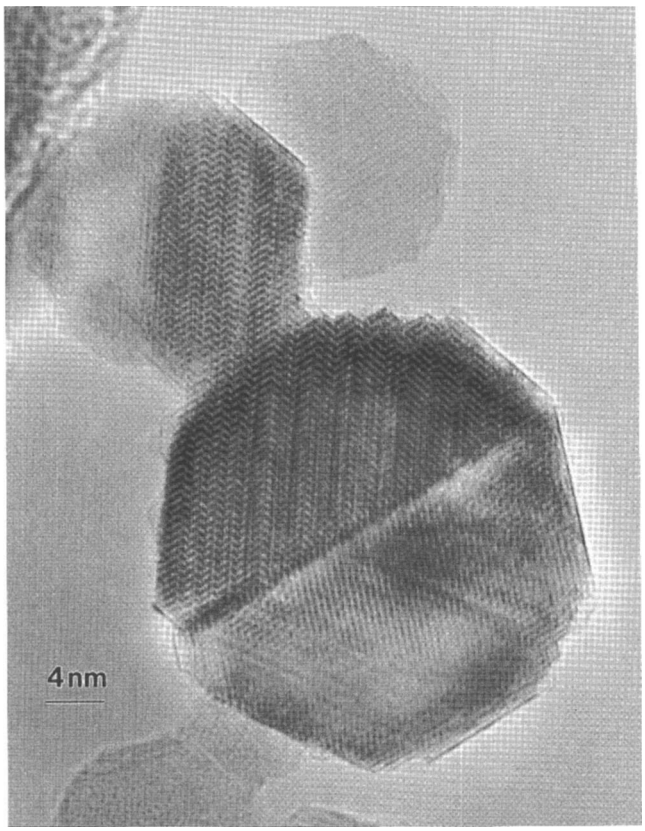

FIG. 13. Two sintered particles that have undergone a transformation to the δ-phase. The smaller particle has grown epitaxially with the larger particle, oriented along $[102]_\delta$. The grain boundary has now migrated inside the smaller particle.

alumina particles have sintered along their {111} facets and, in doing so, appear to have oriented themselves so as to achieve a high degree of coherency across the interface. Such a reorientation is not favored simply because surface diffusion should be sufficiently fast enough to 'lock-in' the initial adhesion orientation. The probability of two particles just adhering and sintering in this orientation is quite low. However, the two particles are clearly distinct (i.e., no grain growth), as indicated by the termination of the {311} lattice planes at the grain boundary. Furthermore, the reconstructed neck region, arrowed, has a different thickness contrast from the 'bulk', suggesting that there exists a slight height difference between the sintered particles.

VI. DISCUSSION

In this study, the sintering of ultrafine particles had dramatically different behavior than the micrometer-sized particles used in traditional sintering models (e.g., Ref. 43). These traditional models require the assumptions of large 'spherical' particles with isotropic surface energy and a chemical potential driving force defined in terms of the neck/particle curvature difference; these

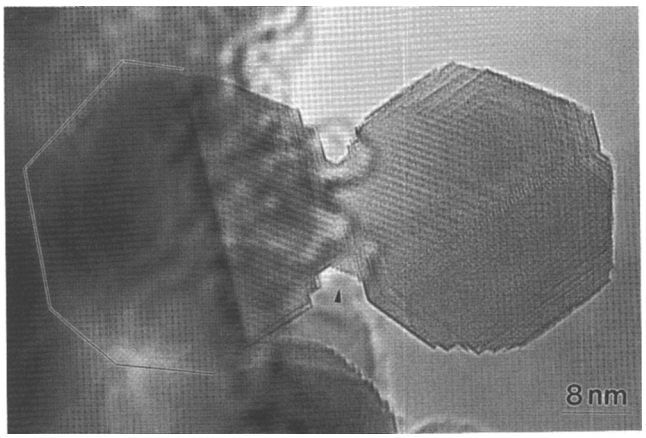

FIG. 14. Two sintered particles of the γ-phase. The neck is sharply faceted and has a discrete contact angle. The particles seem to have phase transformed into one particle; however, closer examination reveals that the {311} planes in the right particle do not cross the grain boundary which also appears as abrupt. Note the neck surface has reconstructed.

models are expected to break down in the case of UFPs where surface properties predominate.

The UFPs have well-defined surface facets which determine the final sintering geometry, thus making surface *energy* considerations, which are necessarily anisotropic, preponderant. In addition, these surface facets result in neck formation which is, even on the atomic level, abrupt having no readily defined radius of curvature. Furthermore, it is likely that the mass transport mechanism that governs the sintering process is surface diffusion. In other words, one would expect surface diffusion to be the 'short-circuit' diffusion path in UFP systems, allowing it to dominate over volume and grain boundary mechanisms. Furthermore, one would not expect significant contributions to mass transport from volume and grain boundary diffusion due to particle size and kinetic effects. Thus, while this study has no direct measurement of diffusion coefficients of any type, it is not unreasonable to conclude that surface diffusion is the predominant mechanism.

Given that the UFPs are out of the range of applicability of traditional sintering models, a different approach must be taken, one that treats the sintering process on the atomic scale. A treatment which seems plausible is to consider the sintering process as the following sequence of steps: (1) The arc discharged particles form well-defined facets consistent with those predicted by the Wulff construction. (2) The particles randomly aggregate in the form of chains; these particle chains then enter the furnace. (3) The chain orientation is 'locked-in' by surface diffusion which is activated as the particles traverse the temperature ramp to the sintering temperature. (4) The UFP chains enter the sintering temperature zone where surface diffusion domi-

nates over grain boundary or lattice diffusion as the mass transport mechanism. (5) The sintered UFPs exit the furnace where the room temperature specimen cartridge quenches the sintering process.

The third step is clearly most important for modeling the initial stages of the sintering process. The question then becomes how to model surface diffusion without having to invoke isotropic surface energy or diffusion coefficients.[44] An appropriate treatment may be found by drawing an analogy to crystal growth from the melt by the mechanism of lateral growth on surfaces. Consider, for example, three ways to achieve growth on surfaces: surface nucleation due to arriving atoms (i.e., evaporation-condensation), spiral growth due to interfacial steps (those supplied by screw dislocations), and growth from twin boundaries.[45] We can neglect the contribution from surface nucleation because there already are thermally activated atoms on the surface which are diffusing. Then we can confine our attention to the spiral and twin growth mechanisms which have similar behavior.

The gist of the model is that when surface diffusion is activated, atoms on the surface have a high degree of mobility and thus mass transport is rapid. Atoms move about on the facets of the UFPs which can be considered as atomically smooth terraces. These 'skating' atoms have, in a simplistic treatment, many dangling bonds, which is energetically unfavorable. Those atoms which happen upon the interface between the UFPs will be energetically driven to the interface in order to reduce their dangling bonds, or, identically, increase their coordination number. Thus the fluxes of atoms about the surfaces of the UFPs are determined by a coordination number gradient where those atoms in the neck region sit in a potential well: a higher binding energy. Also consider that facets such as the {220} represent ideal growth sites being comprised of {111} 'nanofacets' where kinks and jogs are easily found; see, for example, Fig. 14.

Searcy[46] treated the case of aggregates of particles with anisotropic surface energies where the presence of defects (i.e., facets) promoted mass transport. The free energies of the defects were ranked as edge $\geqslant$ ledge $\geqslant$ surface $\geqslant$ grain boundary $\geqslant$ dislocation. Searcy's approach predicts that during sintering the difference in chemical potentials is the driving force for the flux of atoms. An example of this atom flux may be found in Fig. 5 where the middle particle appears to have 'lost' mass, resulting in roughened surfaces on its far side. This roughening would be due to surface diffusion of atoms from the far side to the neck regions with the other two particles. Similar experimental results were observed by Warble[11] during the sintering of γ-alumina.

A complementary interpretation of the UFP sintering process is through the Wulff construction; see Fig. 15. It should be noted that the Wulff construction for the case of multiply-twinned particles has the constraint that the facet surfaces on the twin boundary have to match exactly in order to perform the mathematical cut operation.[47] The grain boundary between two UFPs can also be considered as an internal boundary of a single crystal, e.g., a disclination. We can then model the center-to-center approach of the two UFPs (densification) as the motion of a disclination through a single crystal. The calculations of Ajayan and Marks[48] indicate

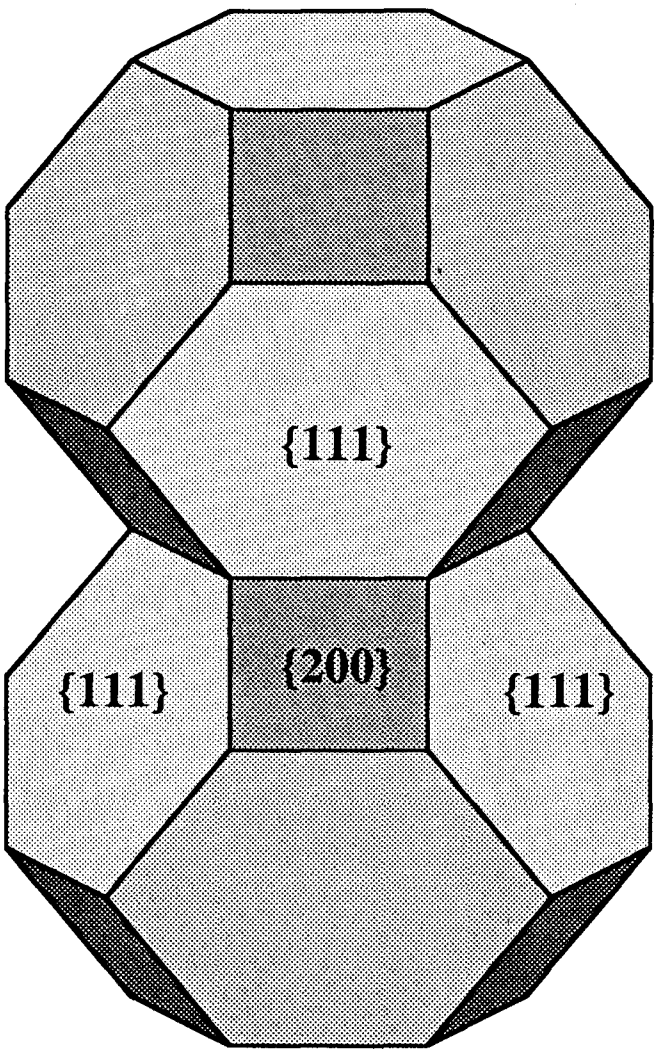

FIG. 15. Two faceted ultrafine particles which have sintered on common {111} facets but with mixed edge character. In this case densification, as defined by center-to-center approach, is constrained by the Wulff construction. In order for the Wulff centers of the particles to approach, the grain boundary must grow in area. That is, the {111} facets must grow at the expense of the {200} facets. However, in this situation, a shrinking {200} facet (labeled) will necessarily cause distortions in the adjacent {111} facets, which is energetically unfavorable and thus no densification occurs. In the presence of an applied stress, the energetic barriers to densification may be overcome.

that there exist cusps, or local minima, in the energy of the particles as a function of the disclination position. These cusps are associated with activation barriers which correspond to the energy cost necessary to move the disclination. Extending this behavior to UFPs suggests that an energy barrier may exist to the center-to-center approach, or densification. That is, the densification process would necessarily cause distortions in the Wulff polyhedra (in order for the facet boundaries to match) and that the driving force for densification is not sufficient to overcome the energy costs of these distortions. Of course, an external force applied to the sintering particles, e.g., pressure, could provide the necessary energy for the densification process to proceed.

Clearly, phase transformations in the UFPs are a concurrent process which has an effect on the sintering behavior. The effects of phase transformations with grain boundary motion have long been noted in the sintering literature. Shingu[49] sintered spheres of Fe with the result that the α- to γ-Fe phase transformation occurred in the sintered compact causing the GBs to migrate freely through the compact so as to bear no relationship to the initial α-Fe boundaries. GB motion has also been noted recently in the case of sintering of α-alumina[50] where 10 nm particles acted as 'seeds' for the recrystallization of larger particles which then grew epitaxially. Though these results are exactly opposite those indicated by Fig. 13, it should be noted those specimens were powder compacts constrained by a heating/deformation holder. The present results represent the sintering of two 'free-body' particles where the smaller particle is clearly not a perfect 'seed' crystal.

It should be noted that in all of the sintering experiments to date, there was no evidence for the formation of the α-phase of alumina. That α-alumina was not observed may be the result of several factors. The temperature required for the equilibrium transformation to α-alumina is at least 1250 °C. It may be that the dwell times used in these experiments were too short to allow the UFPs to complete the transformation, even if the furnace temperature may have exceeded 1250 °C. It may also be possible that under the 'vacuum' conditions (10 kPa) of the sintering experiments that the formation of α-alumina is not favorable regardless of the temperature, or is kinetically limited.[51] This explanation is supported by the results of Iijima[9,10] who sintered UFPs of δ-alumina at 1350 °C for 2 h under vacuum conditions. No evidence was reported of a transformation to α-alumina. Further buttressing this argument, Hirayama[52] sintered Iijima's powders at 1260 °C for 1 h (presumably in 1 atm of argon) and noted the transformation to the α-phase, in addition to the presence of the transition phase aluminas. Furthermore, Warble[11] sintered γ-alumina at 1150 °C for 48 h under atmospheric conditions and observed the transformation to α-alumina.

VII. CONCLUSIONS

Ultrafine particles of alumina were produced by an arc discharge and sintered in a custom-built UHV furnace system under clean conditions. The UFPs have highly faceted surfaces and range in size from 20 to 50 nm with the atomic structure corresponding to variants of the spinel structure. The cubic γ-phase had a lattice parameter of 0.79 nm (*Fd3m*), consistent with previously reported phases. The orthorhombic δ-phase was also observed with lattice parameters of $a_\delta = 1.58$ nm, $b_\delta = 1.17$ nm, and $c_\delta = 0.79$ nm in the $P2_12_12$ space group.

The sintering process in these UFPs demonstrates three major issues: the surface faceting plays a major role in determining the final sintering geometry with sintering occurring predominantly on the close-packed facets (e.g., $\{111\}_\gamma$). The driving force for sintering can be considered as a chemical potential difference between facet surfaces and the neck region. Surface diffusion is the predominant mechanism for mass transport as evidenced by the fact that many sintered particles have their initial adhesion structure 'locked-in' during sintering with no reorientation occurring. Furthermore, the necks formed during sintering have well-defined, atomically sharp contact angles which suggests that the neck growth process is controlled by the faceted structures and may be modeled by a mechanism similar to crystal growth due to ledges, grain boundaries, and twins.

The interface/neck regions that form in between the UFPs may either be atomically abrupt or extended in nature. However, in both cases the neck region is crystalline, and not amorphous. The presence of an 'extended' neck region seems to be more probable when sintering occurs in a cluster of particles, as opposed to two particle sintering where the particles are free to move.

Phase transformations may also occur during the sintering process with the consequence of grain boundary migrations. Transformations to the δ-phase were observed with both grain boundary migrations and crystal growth/grain coalescence competing with the sintering process. No transformations to α-alumina were observed when sintering occurred under 'vacuum' conditions.

In summary, we have investigated the sintering behavior of UFPs under clean conditions in terms of both the atomic structure and particle shape considerations. There remain many more aspects to be studied; for example, the effects of dopants on sintering behavior can be accomplished by alloying the desired additive (i.e., magnesium) in the aluminum electrodes. In addition, the UHV furnace is configured such that it is relatively easy to study the sintering behavior in other materials, say NiO or TiO_2. Further sintering investigations in UFP systems are forthcoming.

ACKNOWLEDGMENTS

This research would not have been possible without the efforts of our colleagues Mao-Hua Teng and D. Lynn Johnson of Northwestern University. This work was supported by the Department of Energy on Grant DE-FG02-87ER45309.

REFERENCES

1. F. R. N. Nabarro, Rept. Conf. Strength of Solids (1948), p. 75.
2. C. Herring, J. Appl. Phys. **21**, 437 (1950).
3. J. Karch, R. Birringer, and H. Gleiter, Nature **330**, 556 (1987).
4. E. O. Hall, Proc. Phys. Soc. London B **64**, 747 (1951).
5. N. J. Petch, J. Iron Steel Inst. **174**, 25 (1953).
6. R. W. Siegel, S. Ramasamy, H. Hahn, L. Zongquan, L. Ting, and R. Gronsky, J. Mater. Res. **3**, 1367 (1988).
7. G. J. Thomas, R. W. Siegel, and J. A. Eastman, Scripta Metall. **24**, 201 (1990).
8. W. Wunderlich, Y. Ishida, and R. Maurer, Scripta Metall. **24**, 403 (1990).
9. S. Iijima, Jpn. J. Appl. Phys. **23**, L347 (1984).
10. S. Iijima, J. Electron Microsc. **34**, 249 (1985).
11. C. E. Warble, J. Mater. Sci. **20**, 2512 (1985).
12. G. W. Nieman, J. R. Weertman, and R. W. Siegel, Scripta Metall. **23**, 2013 (1989).
13. G. W. Nieman, J. R. Weertman, and R. W. Siegel, Scripta Metall. **24**, 145 (1990).
14. G. W. Nieman, J. R. Weertman, and R. W. Siegel, J. Mater. Res. **6**, 1012 (1991).
15. A. H. Chokshi, A. Rosen, J. Karch, and H. Gleiter, Scripta Metall. **23**, 1679 (1989).
16. A. Zangwill, *Physics at Surfaces* (Cambridge University Press, Cambridge, 1988).
17. A. Howie and L. D. Marks, Philos. Mag. A **49**, 95 (1984).
18. J. E. Bonevich, in Proc. 47th Ann. Meet. Electron. Microsc. Soc. Am. (1988), p. 258.
19. K. Kimoto and I. Nishida, Jpn. J. Appl. Phys. **6**, 1047 (1967).
20. C. G. Granqvist and R. A. Buhrman, J. Appl. Phys. **47**, 2200 (1976).
21. T. Hayashi, T. Ohno, S. Yatsuya, and R. Uyeda, Jpn. J. Appl. Phys. **16**, 705 (1977).
22. A. R. Thölén, Acta Metall. **27**, 1765 (1979).
23. K. Heinemann, M. J. Yacaman, C. Y. Yang, and H. Poppa, J. Cryst. Growth **47**, 177 (1979).
24. J. E. Bonevich, M-H. Teng, D. L. Johnson, and L. D. Marks, Review Sci. Instrum. **62**, 3061 (1991).
25. J. E. Bonevich and L. D. Marks, Microscopy (1992, in press); also in Hitachi Instrument News **17**, 4 (1989).
26. There are four cubic 'γ'-phases in Crystal Data: Determinative Tables, 3rd ed., edited by J. D. H. Donnay and H. M. Ondik (JCPDS, 1973), Vol. 2, pp. 35, 189, 195.
27. H. P. Rooksby, *X-ray Identification and Crystal Structures of Clay Minerals* (London, 1951).
28. J. V. Smith, *Geometrical and Structural Crystallography* (John Wiley, New York, 1982).
29. B. C. Lippens and J. H. deBoer, Acta Cryst. **17**, 1312 (1964).
30. H. P. Rooksby and C. J. M. Rooymans, Clay Minerals Bull. **4**, 234 (1961).
31. A. Dauger and D. Fargeot, Radiat. Eff. **74**, 279 (1983).
32. D. Fargeot, D. Mercurio, and A. Dauger, Mater. Chem. Phys. **24**, 299 (1990).
33. V. Jayaram and C. G. Levi, Acta Metall. **37**, 569 (1989).
34. R. Dieckmann, Ber. Bunsenges. Phys. Chem. **86**, 112 (1982).
35. F. Ernst, P. Pirouz, and A. H. Heuer, Philos. Mag. A **63**, 259 (1991).
36. X-ray analysis of UFP specimens conducted by M-H. Teng at Northwestern University.
37. M-H. Teng, Ph.D. Dissertation, Northwestern University (1991), in preparation.
38. J. E. Bonevich and L. D. Marks, Ultramicroscopy **35**, 161 (1991).
39. L. A. Bursill and P. J. Lin, Philos. Mag. A **60**, 307 (1989).
40. I. Hannson and A. R. Thölén, Philos. Mag. A **37**, 535 (1978).
41. A. R. Thölén, in *Microscopic Aspects of Adhesion and Lubrication,* edited by J. M. Georges (Elsevier, Amsterdam, 1982), p. 263.
42. L. D. Marks, Surf. Sci. **150**, 302 (1985).
43. D. L. Johnson, J. Appl. Phys. **40**, 192 (1969).
44. F. A. Nichols, J. Appl. Phys. **37**, 2805 (1966).
45. D. A. Porter and K. E. Easterling, *Phase Transformations in Metals and Alloys* (Van Nostrand, New York, 1981), pp. 199–201.
46. A. W. Searcy, J. Am. Ceram. Soc. **68**, C267 (1985).
47. L. D. Marks, J. Cryst. Growth **61**, 556 (1983).
48. P. M. Ajayan and L. D. Marks, Phase Transitions **24–26**, 229 (1990).
49. P. H. Shingu, Ph.D. Dissertation, Northwestern University (1967), p. 64.
50. M. Komatsu and H. Fujita, Hitachi Instrum. News **21**, 18 (1991).
51. C. J-P. Steiner, D. P. H. Hasselman, and R. M. Spriggs, J. Am. Ceram. Soc. **54**, 412 (1971).
52. T. Hirayama, J. Am. Ceram. Soc. **70**, C122 (1987).